doi:10.26443/seismica.v5i2.2594

Understanding fiber-optic sensitivity to a wavefield: A framework to separate site amplification from orientation effects

Olivier Fontaine * [1], **Andreas Fichtner** [2], **Thomas Hudson** [2], **Thomas Lecocq** [3], **Corentin Caudron** [1]

[1]Laboratoire G-Time, Departement of Geosciences, Environment and Society, Université libre de Bruxelles, 1050 Bruxelles, Belgium, [2]Department of Earth and Planetary Sciences, ETH Zurich, Zurich, Switzerland, [3]Seismology and Gravimetry, Royal Observatory of Belgium, 1180 Uccle, Belgium

Author contributions: *Conceptualization*: O. Fontaine. *Formal Analysis*: O. Fontaine, A. Fichtner, T. Hudson. *Writing - Original draft*: O. Fontaine. *Supervision*: C. Caudron, T. Lecocq.

Abstract When analyzing signals from Distributed Acoustic Sensing (DAS), the recorded amplitude can be difficult to interpret, as it is influenced by many parameters. To explore the foundations of fiber sensing amplitude transfer functions, we first generalize existing sensitivity expressions to arbitrary fiber orientations. Building from those, we characterize DAS sensitivity at the scale of the full deployment and investigate the influence of a layered medium. Finally, we demonstrate how loop gauge length could suppress shear waves polarized in the plane of the loop. From these transfer functions, we explore the wavefield as seen by DAS through a forward model based on ray theory. This model predicts the distribution of amplitude measurements along the fiber from a point source at low computational cost. Comparing the predicted and observed wavefields provides an estimate of local amplification effects. The proposed framework provides the basis for a wide range of applications, including fiber deployment optimization, synthetic DAS generation, and amplitude-based grid search.

Production Editor: Gareth Funning
Handling Editor: Wenbo Wu
Copy & Layout Editor: Hannah F. Mark

Signed reviewer(s): Ethan Williams

Received: February 2, 2026
Accepted: October 30, 2026
Published: November 26, 2026

1 Introduction

The rapid advancement of distributed acoustic sensing (DAS) is transforming the field of seismology. This technology enables the conversion of optical fibers into arrays of thousands of seismic sensors, pushing the frontiers in Earth sciences, including monitoring of volcanic and glacial processes (Walter et al., 2020; Hudson et al., 2020; Fichtner et al., 2023; Jousset et al., 2025; Nakano et al., 2024; Fichtner et al., 2026), and the early detection of earthquakes and tsunamis (Yin et al., 2023; Lior et al., 2021). However, the nature of the wavefield sensed by DAS differs from the displacement sensed by seismometers (Capdeville and Sladen, 2024; Kennett, 2024).

To convert optical fibers into seismic sensors, DAS interrogators inject coherent laser pulses at one end of the fiber. As the pulse travels in the fiber, small defects in the crystalline lattice scatter the light, allowing a fraction of the light to travel back to the interrogator. Phase shifts in the backscattered light, caused by relative displacements of the scatterers within the fiber, are measured by the interrogator (Hartog et al., 2014). The locations of these perturbations are then determined from the two-way travel time of the laser pulse. Therefore, compared to displacement, DAS measures strain, a spatial derivative in the fiber direction (Daley et al., 2014), whereas seismometers record velocity, a time derivative of displacement. In practice, however, some DAS interrogators, including the one used in this study, output strain rate rather than strain. The relations between these measurement units and their respective sensing methods are portrayed in Figure 1. This discrepancy in derivation is at the core of the unique sensitivity of axial strain sensing as observed already by Benioff (1935) and later in numerous DAS publications (Daley et al., 2014; Bakku, 2015; Wang et al., 2018; Vera Rodriguez and Wuestefeld, 2020; Martin et al., 2021; Kennett, 2024).

The strain recorded by DAS may vary as a function of several parameters. First, the interrogator averages the phase over a segment of the fiber, called a gauge length. This imposes a filter in the wavenumber domain, with a sinus cardinal (sinc) transfer function (Vantassel et al., 2022), effectively attenuating components of the wavefield whose wavelengths correspond to even fractions of the gauge length (Lindsey et al., 2020; Walter et al., 2020; Martin

*Corresponding author: olivier.fontaine@ulb.be

et al., 2021). Other parameters such as the fiber casing (Jiang et al., 2023), tension in the fiber (Xie et al., 2022), its coupling with the surrounding medium (Daley et al., 2014; Ajo-Franklin et al., 2019; Walter et al., 2020; Hudson et al., 2025b), as well as the physical properties of the medium itself (Celli et al., 2024; Ma et al., 2024), may also play non-negligible roles. Furthermore, recent studies suggest that the strain wavefield has a strong response to heterogeneity in the earth's subsurface much smaller than the minimum considered wavelength (Paitz et al., 2020; Capdeville and Sladen, 2024).

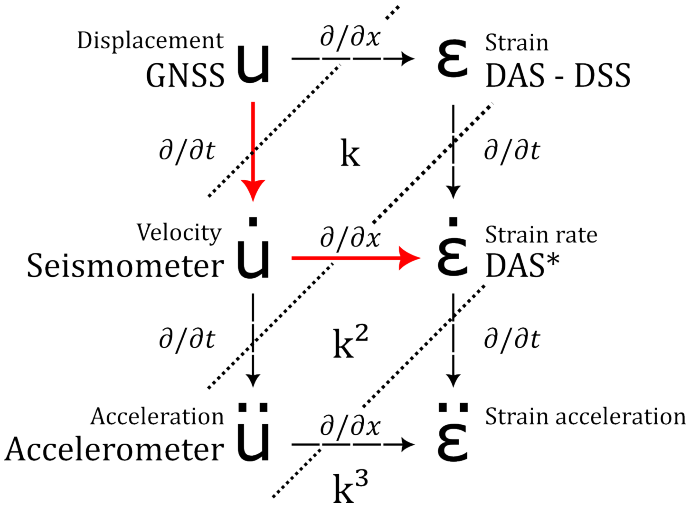

Figure 1 Relation between displacement (u) and strain (ϵ) with their relative time derivative and their means of measurement. Oblique delimitations isolate units with a similar number of derivatives and thus similar number of multiplications by the wavenumber (k) on their spectrum. Native DAS measurements are proportional to strain through optical phase changes. However, many interrogators, like the Silixa iDAS, output the data in strain rate (DAS*). DSS refers to Distributed Strain Sensing.

The interplay of these parameters and the vast range of deployment possibilities highlight the importance of accurately understanding the transfer function of DAS. This is particularly relevant for methods that depend on amplitude measurements, such as full-waveform inversion (Hudson et al., 2020; Luo et al., 2021; Noe et al., 2026), or amplitude-based event location (Nishimura et al., 2021). Moreover, understanding this transfer function can be leveraged to reduce the volume of data by focusing only on source-specific sensitive segments of the cable or guide future deployments through optimized fiber geometries (Fichtner and Hofstede, 2023).

Up to now, studies quantifying DAS amplitude and local amplification effects can be split into two categories. The first uses the Array-Derived Dynamic Strain (ADDS), while the second is based on the Discrete Particle Scheme (DPS). The first method, ADDS, reconstructs the strain rate wavefield using a co-located seismometer array (Wang et al., 2018; Currenti et al., 2021; Ichinose et al., 2022; Muir and Zhan, 2022). This approach was adopted in the early stages of DAS to assess the quality of the recorded waveforms using seismometers, as in Daley et al. (2016). In volcanic terrains, discrepancies between ADDS and DAS measurements were attributed to the presence of faults (Currenti et al., 2021). In the second method, DPS, the medium and the fiber are modeled by a network of interconnected particles. By changing the quality of the elastic bonds linking these particles, the local fiber response to a wavefield can be obtained (Jiang et al., 2023; Celli et al., 2024; Hudson et al., 2025b).

However, these two methods may not be adequate to keep up with the rapidly increasing diversity of fiber deployments. For instance, limitations arise when no seismic array with adequate geometry is available, or when elastic properties of the medium cannot be determined at a scale comparable to the high spatial resolution of DAS with an approachable computational cost. To build on the idea proposed in Kennett (2022), we address this gap in comparative measurements by examining the wavefield as it is "seen" by DAS, and compare a theoretical amplitude distribution along the fiber with actual recordings for a given source. The mismatch between the theoretical and the recorded amplitude distribution provides a lumped estimate of the local DAS response along the fiber, integrating the combined influence of near-surface effects, small-scale heterogeneity, cable coupling, and spatial variations in the elastic properties of the medium itself encompassing free-surface effects.

2 Data and method

2.1 DAS sensitivity

To understand how different waves coming from different directions are recorded by DAS, we examine the axial strain rate expression for different wave polarizations and fiber orientations. The full demonstration of those equations along with a visualization of the coordinate system can be found in the supplementary materials.

To formulate our expression, we consider a plane waves propagating in direction $\vec{K}$ as described in equation 1, with φ_r and θ_r the azimuth and the dip of the ray, both defined to progress in trigonometric direction.

$$\begin{aligned}\vec{K} &= [k_x, k_y, k_z] \\ &= k[\cos(\varphi_r)\cos(\theta_r), \sin(\varphi_r)\cos(\theta_r), \sin(\theta_r)]\end{aligned} \tag{1}$$

For this plane wave, we define a set of displacement polarization vectors for P, SV, and SH waves that are derived in time and then in space along the xx axis to get the axial strain rate in the fiber axis. In this last step, we integrate two rotations to the strain tensor to align the xx component with any azimuth (φ_D) and dip (θ_D) of the fiber segment, becoming the xx' direction. The DAS azimuth and dip are also defined to progress in trigonometric directions. This gives us equations 2, 3, and 4 for point strain rate:

$$\dot{\epsilon}^{P}_{xx'} = k^2 cA\big(\cos\theta_D\cos\theta_r\cos(\varphi_D-\varphi_r) + \sin\theta_D\sin\theta_r\big)^2\psi(x,y,z,t) \tag{2}$$

$$\dot{\epsilon}^{SV}_{xx'} = k^2 cA\big(-\cos\theta_D\sin\theta_r\cos(\varphi_D-\varphi_r) + \sin\theta_D\cos\theta_r\big)\big(\cos\theta_D\cos\theta_r\cos(\varphi_D-\varphi_r) + \sin\theta_D\sin\theta_r\big)\psi(x,y,z,t) \tag{3}$$

$$\dot{\epsilon}^{SH}_{xx'} = k^2 cA\cos\theta_D\sin(\varphi_r-\varphi_D)\big(\cos\theta_D\cos\theta_r\cos(\varphi_D-\varphi_r) + \sin\theta_D\sin\theta_r\big)\psi(x,y,z,t) \tag{4}$$

with the wave displacement amplitude A, the oscillatory term $\psi(x,y,z,t)$ as defined in equation 5, the phase velocity c, and wavenumber k.

$$\psi(x,y,z,t) = e^{ik(ct - x\cos(\varphi_r)\cos(\theta_r) - y\sin(\varphi_r)\cos(\theta_r) - z\sin(\theta_r))} \tag{5}$$

Then, to consider the gauge length effect, we average these equations over a linear segment in the fiber orientation rendering equations 6, 7, and 8.

$$\begin{aligned}\dot{\epsilon}^{P}_{xx'g} =& \frac{2cA}{g}\big(\cos\theta_D\cos\theta_r\cos(\varphi_D-\varphi_r) + \sin\theta_D\sin\theta_r\big) \\ &\times \quad \sin\left[\frac{kg}{2}\big(\cos\theta_D\cos\theta_r\cos(\varphi_D-\varphi_r) + \sin\theta_D\sin\theta_r\big)\right]\psi(x,y,z,t)\end{aligned} \tag{6}$$

$$\begin{aligned}\dot{\epsilon}^{SV}_{xx'g} =& \frac{2cA}{g}\big(-\cos\theta_D\sin\theta_r\cos(\varphi_D-\varphi_r) + \sin\theta_D\cos\theta_r\big) \\ &\times \quad \sin\left[\frac{kg}{2}\big(\cos\theta_D\cos\theta_r\cos(\varphi_D-\varphi_r) + \sin\theta_D\sin\theta_r\big)\right]\psi(x,y,z,t)\end{aligned} \tag{7}$$

$$\begin{aligned}\dot{\epsilon}^{SH}_{xx'g} =& \frac{2cA}{g}\cos\theta_D\sin(\varphi_r-\varphi_D) \\ &\times \quad \sin\left[\frac{kg}{2}\big(\cos\theta_D\cos\theta_r\cos(\varphi_D-\varphi_r) + \sin\theta_D\sin\theta_r\big)\right]\psi(x,y,z,t)\end{aligned} \tag{8}$$

As suggested in Hudson et al. (2025a), a generalized S wave sensitivity can be obtained by combining the two polarizations using $\sqrt{\dot{\epsilon}^2_{xx'SHg} + \dot{\epsilon}^2_{xx'SVg}}$. Lastly, following Martin et al. (2021), for a wavelength much larger than the gauge length, its effect can be neglected and DAS strain rate is close to pointwise strain rate.

In these equations (2, 3, 4, 6, 7, 8) the axial strain rate amplitude is controlled by quantities such as the wavenumber, gauge length, and velocity. In addition, and central to this paper, it is affected by a geometric effect arising from the relative orientation between the fiber and the wavefield. Hereafter, this angular dependence is referred to as the fiber sensitivity. It plays a key role in the characterization of DAS angular sensitivity, regardless of whether the DAS response is expressed in terms of strain or strain rate. To illustrate this term we suggest three kinds of visualization visible in Figure 2, for a fiber along the y-axis (azimuth = 0°) with a dip of 45°. In the left column, we consider this sensitivity from a source perspective. In a homogeneous 1 km^3 cube , with the fiber in its center, we distribute sources evenly throughout the surrounding space. Each pixel in this space contains a source and is colored following the amplitude it can generate in the fiber for a specific polarization, using a straight ray. When plotting our cubes, only the outer surfaces are colored to enhance visibility. In the central column, the same geometrical factor is visualized as a volume surrounding the fiber. Lastly, in the right column we suggest a polar projection, with the center con-

taining rays coming from the bottom. The outer rim contains the rays coming from the top. We also normalized the amplitude to 1 to the maximum value on each display.

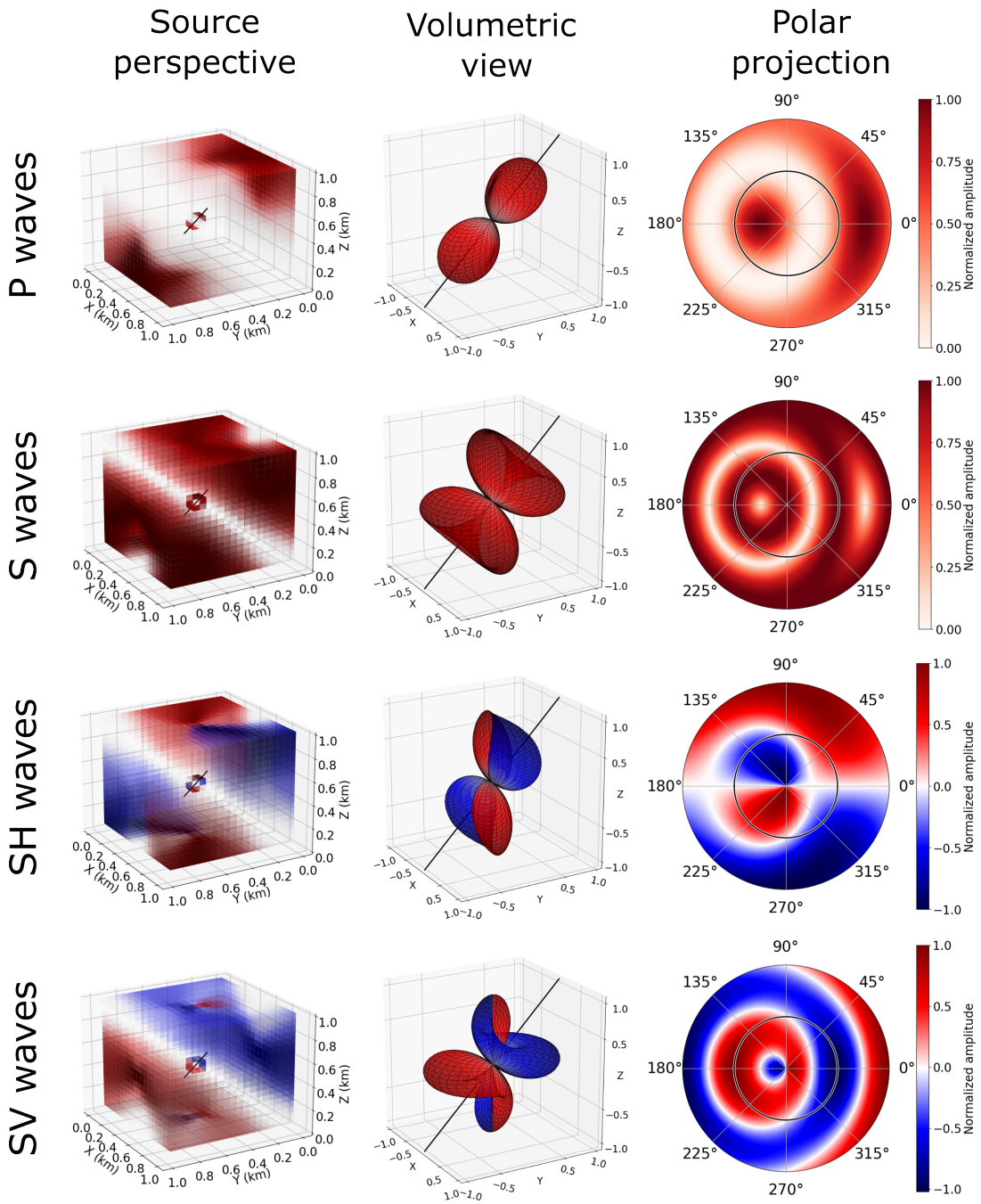

Figure 2 Representation of the angular sensitivity of a fiber to body waves. The fiber, shown as a black line in the left and central columns, has a dip of $45°$ and an azimuth of $0°$. The representations are based on equations 2, 3, and 4 and consider a wavelength much larger than the gauge length. The S-wave amplitude is computed as $\sqrt{\dot{\epsilon}^2_{xx'SH} + \dot{\epsilon}^2_{xx'SV}}$. The left column illustrates the sensitivity for sources homogeneously distributed around the fiber in a homogeneous medium; each pixel is colored according to the amplitude recorded by the fiber in the center of the cube for a source located at the pixel for a given polarization. The central column presents a volumetric representation of the fiber angular sensitivity to body waves, while the right column shows the corresponding polar projections. In these polar plots, rays arriving from below are mapped to the center, horizontal rays are indicated by the black circle, and vertically incident rays from above are located at the outer rim. All plots are normalized by their respective maximum values.

For both P and S waves, the sensitivity preserves its 2D relation of $\cos^2(\varphi_r)$ and $\sin(2\varphi_r)$, but forming a solid of revolution around the fiber axis. This relation is clearly visible in the volumetric view, in the central column of Figure 2. However, the relative contributions of the SV and SH components vary significantly with the dip. As the sensitivity to SH waves decays proportionally to $\cos(\theta_D)$, it will reach zero for a vertical fiber. Consequently, SV waves exhibit a strong azimuthal constraint for a horizontal fiber. This azimuthal constraint gradually disappears as the fiber dip

increases, resulting in sensitivity to all azimuths for a vertical fiber. The equations 3, 4, 7, and 8 also predict the spatial distribution of polarity reversal for the different shear-wave polarizations. This complex sensitivity to shear waves can yield strong information on the source orientation as in Luo et al. (2021) but requires acute knowledge of the fiber geometry.

2.2 Integration of DAS sensitivity in a ray based framework

In this section, we expand beyond a plane wave sensitivity model from the last section, to consider an arbitrary source mechanism. For this, we integrate our sensitivity analysis to a wavefield framework based on ray theory, accounting for various source descriptions.

To model the propagation of waves, we use Pykonal (https://malcolmw.github.io/pykonal-docs/). This open-source Python package is designed to calculate travel-time grids by numerically solving the Eikonal equation using the Fast Marching Method (FMM) (White et al., 2020). This method enables efficient computation of first-arrival travel times in both 2D and 3D domains, supporting spherical and Cartesian coordinate systems. To propagate rays through the travel time grid, Pykonal uses the path of steepest descent, from the source to the receiver using Euler's steps (White et al., 2020). Compared to traditional ray-based approaches, like the shooting or bending methods, a grid-based approach offers greater numerical stability and is well suited to handle complex 3D velocity models (Rawlinson et al., 2008). However, by design, it can only account for the first arrival.

To implement this framework to our test case, Brady Hot Springs (BHS), we used the 3D velocity model from Matzel et al. (2017), with an original resolution of 25 m. To ensure that the high-frequency assumption required for ray theory, we applied a low-pass filter to the velocity model, with 99% attenuation at 10 wavelengths (Liu and Schmitt, 2006). The filter parameters are based on a 5 Hz signal (see Section 2.3) traveling at 0.6 km/s. Based on the synthetic tests presented in the supplementary materials, we estimated uncertainties of 0.59° at the source and 3.30° at the receiver for the ray parameters. These values were incorporated into a Monte Carlo error-propagation scheme, resulting in an average forward-model amplitude uncertainty of 17.9%.

Finally, to describe the source, we used the direction- and polarization-dependent radiation amplitudes of a single force given by equation 4.23 of Aki and Richards (2002). For our model, to keep the polarization simpler, we used a far field approximation. Therefore to reduce the influence of the near field in the data, important for the region with source-receiver distance equal or smaller than a wavelength (Lokmer and Bean, 2010), we kept the data in its original unit, strain rate. Owing to the spatial derivative to move from velocity to strain rate, visible in Figure 1, the resulting spectrum is closer to acceleration, decreasing low frequency, therefore long wavelength, amplitudes.

2.3 DAS Data measurement and processing

To validate the amplitude model developed in this study, we use data from the Poroelastic Tomography experiment (PoroTomo) (Feigl, 2019). This open dataset includes a DAS fiber deployed in 2016 at the Brady Hot Springs geothermal field (Nevada, USA). The fiber (DASH) was installed in a zigzagging trench at 1 m depth, visible on Figure 3, providing a wide range of orientations suitable for testing angular sensitivity. The site consists of a Mesozoic crystalline basement (~1400 m depth) overlain by Miocene to Pleistocene sedimentary and volcanic deposits, capped by a ~50 m sedimentary cover, identified by strong velocity contrasts in Matzel et al. (2017); Siler and Pepin (2021). The area is crosscut by SSW–NNE-trending normal faults, which have been shown to significantly affect DAS strain amplitudes (Jousset et al., 2018; Currenti et al., 2021; Ma et al., 2024).

The PoroTomo experiment recorded a variety of signals from active vibroseis sources and natural seismicity (Wang et al., 2018). In this study, we focus on the active-source dataset, which comprises 6633 cataloged events with well-constrained source locations and mechanisms. The vibroseis signals consist of 20 s sweeps spanning 5–80 Hz. We analyze nine source sites distributed across the array, visible on Figure 3, each including nine sweeps of three types: compressional (P), shear transverse (ST), and shear longitudinal (SL), with three repetitions per type at each site.

These signals were recorded using a Silixa iDAS with a gauge length of 10 m and a spatial sampling of 1 m at 1 kHz. Preprocessing includes removing common-mode noise (Lindsey et al., 2020) and applying a bandpass filter between 3 Hz and 20 Hz. To enhance the signal-to-noise ratio (SNR) and reduce the volume of data, channels are grouped and linearly stacked in sets of 11. Then we downsample after band passing, using a mean, to 100 Hz.

After preprocessing, we used a trigger on each sweep to capture the onset of the signal. For this, we employed the Modify Energy Ratio (MER) from Han et al. (2009). Because of the large energy difference between the channels, up to 22.69 dB across tens of channels, as can be seen in Figure 4, identifying a fixed threshold for a trigger proved challenging and those had to be re-optimized for each event. Instead, we chose the percentiles 65 of the MER values for each DAS channel, to achieve a data-driven trigger level. To ensure the quality of the picking, each trigger must

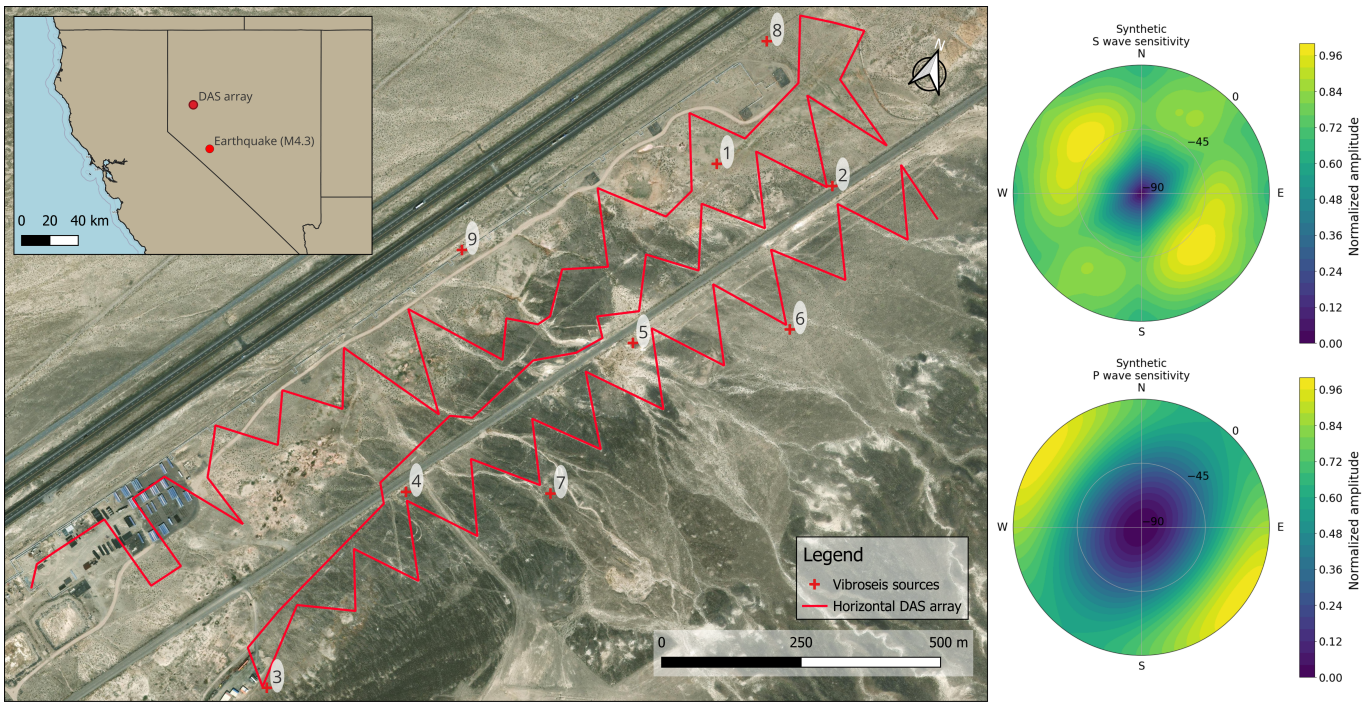

Figure 3 Map of the PoroTomo DAS fiber deployment (red line) and the Vibroseis sources used in this study (red crosses). The top-left inset shows the location of Brady Hot Springs in Nevada, as well as the location of the magnitude 4.3 earthquake used to compare our site amplification analysis. On the right, the synthetic spatial sensitivity for the PoroTomo horizontal DAS array, illustrating the directional response to seismic waves as a function of azimuth and incidence angle (dip). The top polar plot shows the corresponding average S-wave sensitivity across all individual channels in the array, while the bottom polar plot presents the average P-wave sensitivity. Both polar plots are normalized by their respective maximum values.

be within 0.5 s of its neighbors and 3 s of the mean timestamp of all triggers. Those not meeting these criteria are redefined as a linear interpolation of the two closest valid triggers. After obtaining the initial arrivals, the signal amplitude is measured using a 0.3 s RMS window. An example of these triggers and quality criteria are displayed in Figure 4. To ensure that the amplitude measured is the one of the passing wavefield and not a local noise source, only channels with an SNR greater than 2 are included in the analysis.

3 Results

From the equations of axial strain-rate sensing, we will look at DAS angular sensitivity from two complementary perspectives. First, we consider the problem from the fiber's point of view across three spatial scales. At the array scale, we assess the directional sensitivity of the entire fiber. We then focus on the channel scale, where we investigate the response of an individual DAS channel embedded in a more complex medium. Finally, at the gauge-length scale, we demonstrate how strain polarity reversal can be used to produce a shear wave polarity filter. Second, we adopt the perspective of a seismic source illuminating the fiber array. This approach provides insight into how a simplified wavefield would be recorded along the fiber and allows us to identify and quantify local amplification effects.

3.1 From the fiber to the space around it

3.1.1 DAS array summary

To assess the overall angular sensitivity of a DAS array, we construct a synthetic sensitivity polar projection by averaging the individual responses of all channels. An example for the DASH from PoroTomo is presented in Figure 3 for both P and S waves.

Based on the BHS fiber layout, P waves should be, on average, better recorded if traveling horizontally in the NW-SE axis, with an overall poor recording for steep rays. In comparison, S waves can be recorded at a much steeper angle, with a maximum at around 45° in the NW-SE direction. For both polarizations, a perfectly vertical ray should not be recorded if we only consider the direct axial strain rate. We also note that these projections do not inform us about the influence of any local velocity structure .

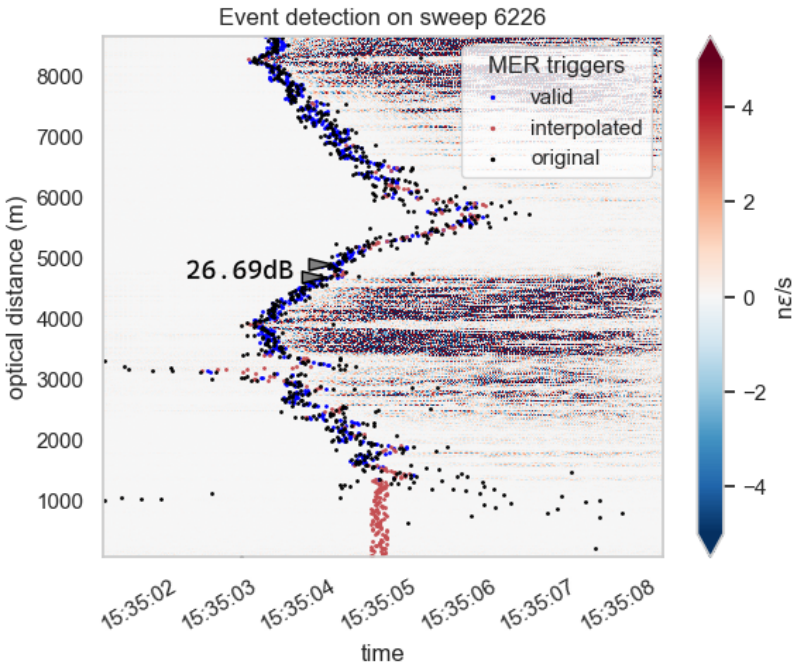

Figure 4 Example of a DAS record (Sweep 6226, Site 2) expressed in nanostrain rate ($n\epsilon/s$) with triggers obtained using the Modified Energy Ratio (MER). The original triggers are shown as black dots. Blue dots indicate valid triggers, while red dots represent interpolated triggers. The amplitude difference of 26.69 dB is measured between 4634 m and 4997 m.

3.1.2 Impact of a layered medium on fiber sensitivity

Using our ray-based DAS sensitivity framework, we investigate how a layered velocity model influences the spatial distribution of source sensitivity for different fiber orientations.

Our model consists of a 1 km^3 cube divided into two layers of equal thickness, with the upper layer having a seismic velocity 50% lower than the underlying one. A fiber is embedded within the upper layer and oriented along the y-axis. To investigate the effect of fiber dip on the spatial sensitivity, we consider three configurations: a horizontal, 45° dipping, and vertical fiber. Sources are distributed uniformly throughout the cube, and for each we perform a ray tracing. Then its location is colored according to the amplitude recorded by the fiber for a given wave polarization. In this analysis, only the angular sensitivity of the DAS response is considered, and all sensitivity kernels shown in Figure 5 are normalized to a maximum amplitude of one.

From a ray perspective, the presence of a shallow low-velocity layer focuses rays that cross the boundary into a narrow range of steep angles, distorting the mapping between the DAS angular sensitivity illustrated by the polar subplots in Figure 5, and source back azimuth and elevation. This behavior provides a useful framework for interpreting the spatial patterns of source sensitivity observed in the sensitivity kernels shown in Figure 5.

In the left column, we see the response for a horizontal fiber. Both P and SH waves exhibit their highest sensitivity for rays propagating horizontally. As a result, the refraction induced by the velocity contrast produces a strong drop of recovered amplitude for sources located beneath the interface. The effect is the strongest for P waves and has been observed in some DAS deployments (Kennett, 2022; Hudson et al., 2021). In contrast, SV waves are better recovered for steeper angles, with a maximum at 45°. In the kernel, this translates to a broadening of the footprint of the sensitive region in the lower layer.

The central column illustrates the intermediate case of a fiber dipping at 45°. P-wave sensitivity remains strongest for rays arriving in the fiber axis. The SV-wave response, however, exhibits a more complex structure with its 4 distinct lobes merging at steeper incidence angles. The projection of those and their relative shadow zones in the kernel create an asymmetrical sensitivity between the two layers. On the other hand, SV waves are well recovered if traveling horizontally or vertically. The kernel shows strong sensitivity in the top layer and directly underneath the fiber, the velocity contrast broadening the shadow zones in the rest of the lower layer.

Lastly, for a vertical fiber in the right column. As expected in the equations 4 and 8, no vertical strain is generated by SH waves. P and SV waves exhibit reduced sensitivity to horizontally propagating rays as observed in Mateeva et al. (2014), producing a broad shadow zone throughout the upper layer. Concerning the sensitivity to the lower space, we reach a limitation of the kernel visualization. On one hand, P wave sensitivity is strong on the entire lower layer, getting stronger for sources beneath the fiber. In contrast, SV-wave amplitudes are strongest away from the fiber axis

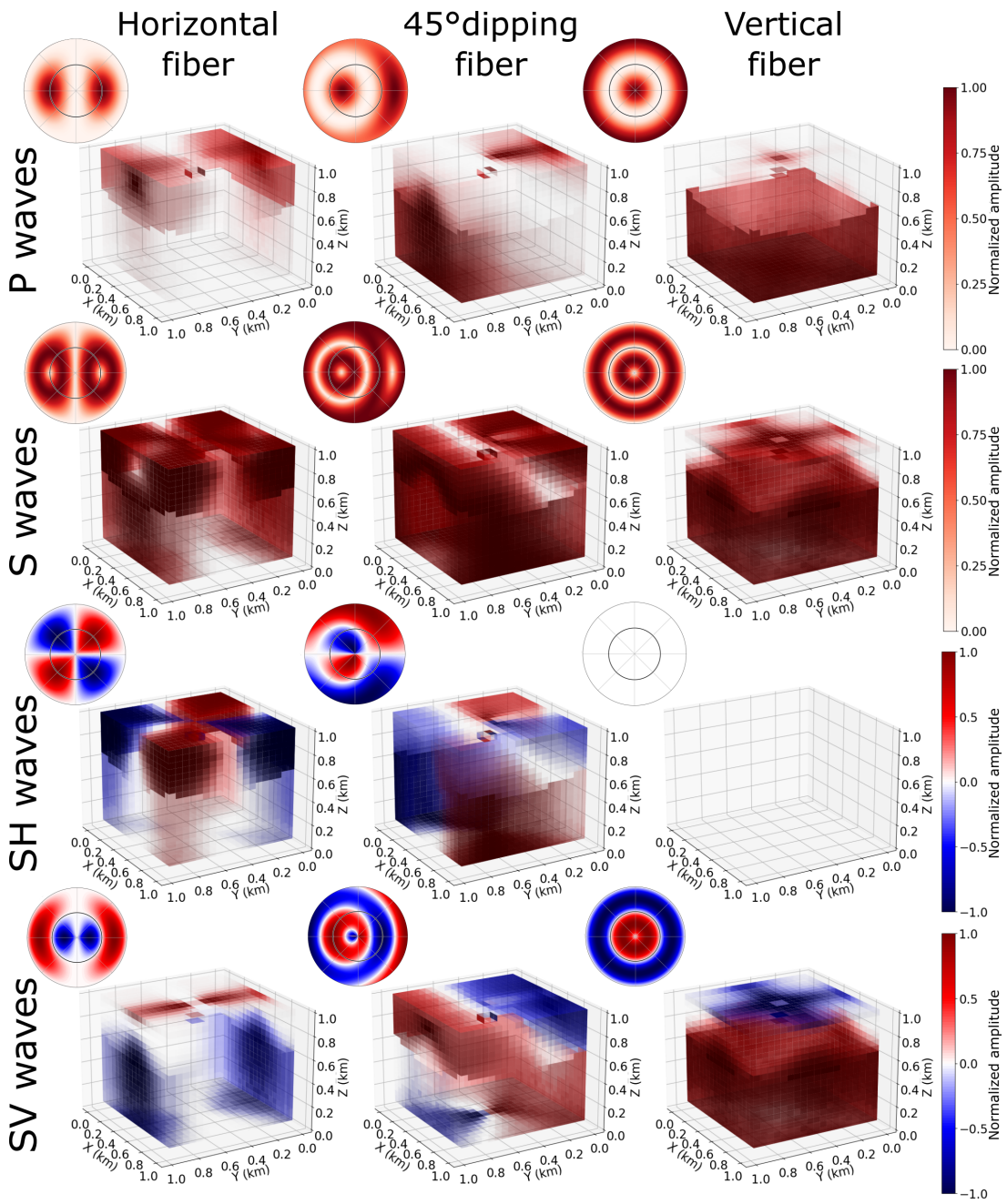

Figure 5 Sensitivity kernel for a fiber in a layered medium compared to its angular sensitivity. The kernels are built using a 1 km^3 volume divided into two layers of equal thickness, with the seismic velocity in the top layer set to 50% lower than in the lower layer. Each pixel is colored according to the ability of a source at that location, for a given body-wave polarization, to generate strain in the fiber. For each polarization, 3 DAS channel orientations are considered: horizontal (left), 45° dip (center), and vertical (right). Therefore, the central column is the equivalent of the left one in Figure 2 with the introduction of a velocity contrast. For each sensitivity kernel, only the outer surface of the volume is displayed for clarity, and its maximum value is normalized to one. Angular sensitivity of the fiber is portrayed in a polar projection of the top left of each kernel. Rays coming from below are mapped at its center while rays coming from the top correspond to the outer rim.

and vanish for vertically propagating rays. The velocity contrast consequently broadens the footprint of the inline P wave sensitivity and the SV waves shadow zone in the lower layer. Combining the SH and SV responses into a total S-wave sensitivity reveals a maximum response for rays propagating at 45° from the fiber axis. The influence of the velocity contrast is particularly apparent. For a horizontal fiber, refraction enhances the sensitivity to the lower layer primarily through the SV contribution. As the fiber dip increases, the low-sensitivity region aligned with the fiber axis is projected in the lower space, with the velocity contrast broadening the footprint of the shadow zone in the lower space.

This model, although simplistic, highlights the complexity of strain measurement and how the orientation of the fiber may constrain the sensitivity to certain regions of the space. However, in the case of a fiber with known

geometry, this complexity can be turned in information as the relative presence of certain phases in sections of the cable can inform on the potential location of the source. This idea has already been explored in Hudson et al. (2025a) and could be carried further using these models. Moreover, even though this section focused on the amplitude, these equations also predict the spatial distribution of S-wave polarity reversals. This information can be incorporated in array processing techniques such as slant-stacking by assigning the predicted amplitude sign for each channel to the corresponding element of the steering vector, to account for the DAS transfer function. This has been used for shear-wave splitting analysis (Hudson et al., 2021) and plane-wave beamforming (Lindsey et al., 2017). Furthermore, these polarity reversal could be used at the scale of the gauge length to filter out some parts of the wavefield, using, for instance, looped gauge lengths.

3.1.3 Looped Gauge Length

Since DAS transfer function can induce polarity reversal and a gauge length averages the wavefield over a segment of fiber, we could turn this uniqueness in an analog polarity filter. This is done by looping the gauge length in the horizontal or vertical plane, to average the wavefield over all azimuths or dips, respectively.

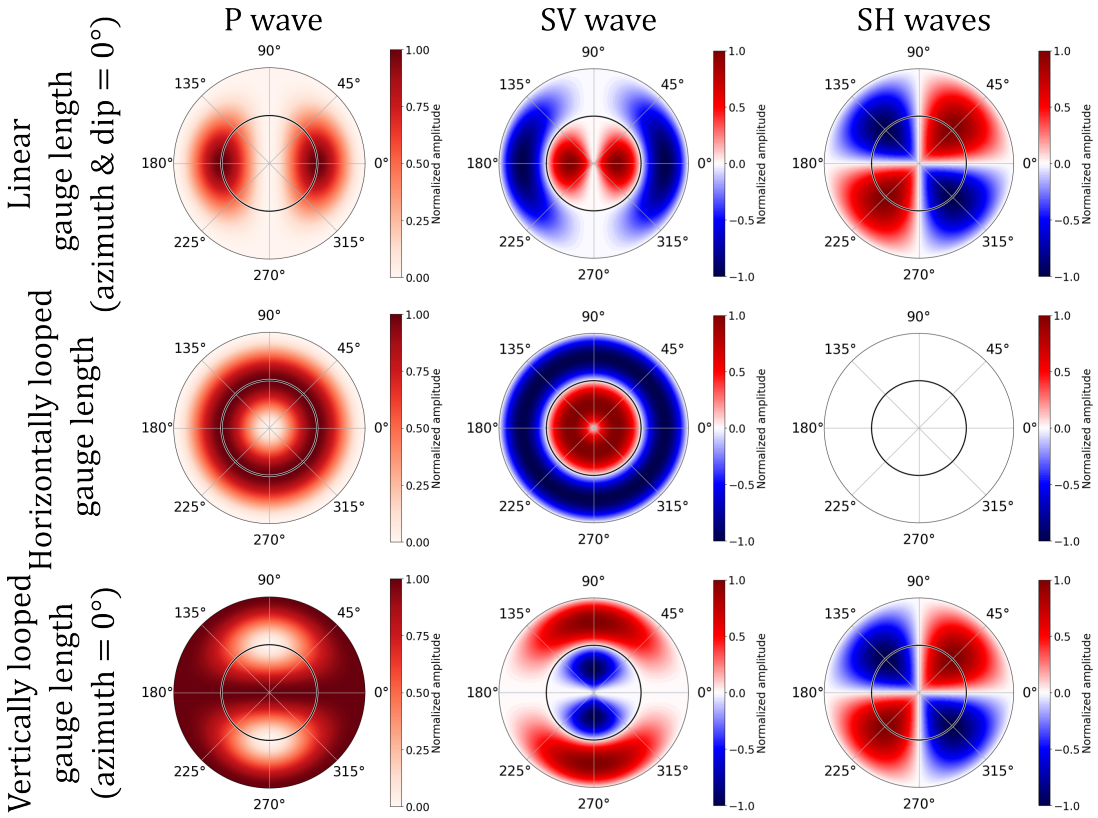

Figure 6 Orientation specific amplitude response of looped and linear gauge length to body waves. These figures are based on the equations 9, 10, and 11 for a vertical loop and 12, 13, and 14 for a horizontal loop. These equations consider a wavelength much larger than the gauge length. In these polar plots, rays arriving from below are mapped to the center, horizontal rays are indicated by the black circle, and vertically incident rays from above are located at the outer rim. All plots are normalized by their respective maximum values.

To build these new expressions we started from the equations 2, 3, and 4, for a linear fiber. For simplicity, we assume a large wavelength-to-gauge length ratio such that the DAS response approaches a point strain rate measurement. The loop, of radius R, is made to have a perimeter equal to a gauge length so $g = 2\pi R$. For a vertical loop, we average over all dips by solving $\frac{1}{2\pi R}\oint \dot{\epsilon} R d\theta_D$ for P, SV and SH waves yielding equations 9, 10, and 11 respectively.

$$\dot{\epsilon}_{vl}^{P} = \frac{k^2 cA}{2}(\cos^2(\theta_r)\cos^2(\varphi_D - \varphi_r) + \sin^2_{\theta_r})\psi(x,y,z,t) \tag{9}$$

$$\dot{\epsilon}_{vl}^{SV} = \frac{k^2 cA}{4}\sin(2\theta_r)\sin^2(\varphi_D - \varphi_r)\psi(x,y,z,t) \tag{10}$$

$$\dot{\epsilon}_{vl}^{SH} = \frac{k^2 cA}{4}\cos(\theta_r)\sin(2(\varphi_D - \varphi_r))\psi(x,y,z,t) \tag{11}$$

For a horizontal loop we average over all azimuth using $\frac{1}{2\pi R}\oint \dot{\epsilon} R d\varphi_D$, for P, SV and SH waves giving equations 12, 13, and 14.

$$\dot{\epsilon}^{P}_{hl} = \frac{k^2 cA}{2}\cos^2(\theta_r)\psi(x,y,z,t) \tag{12}$$

$$\dot{\epsilon}^{SV}_{hl} = -\frac{k^2 cA}{4}\sin(2\theta_r)\psi(x,y,z,t) \tag{13}$$

$$\dot{\epsilon}^{SH}_{hl} = 0 \tag{14}$$

The resulting expressions are visualized in Figure 6, with detailed derivations provided in the supplementary materials.

Based on these new equations, in the case of a horizontal loop, the sensitivity to both P and SV waves loses its azimuthal constraint, while the dip dependency remains unchanged. In contrast, SH waves are effectively canceled due to the average with the polarity reversal. For a vertically oriented loop, P-waves retain their typical azimuthal sensitivity, but it becomes distributed across all dip angles. SH waves exhibit a similar response as in a horizontal linear fiber. SV waves, however, appear to be canceled in the loop direction, yet new sensitivity lobes emerge at a $\pm 45°$ dip to the normal of the plane containing the loop.

Overall, the gain in angular sensitivity to P waves in a looped fiber was already observed in Kuvshinov (2016) for a wrapping angle of 89°. On the other hand, we demonstrate the lack of sensitivity of the fiber loop to shear waves polarized in its plane. It is a direct consequence of the divergence-free nature of the shear-wave displacement field. For a linear fiber segment, this manifests as a polarity reversal for different arrival angles, that cancel out on a loop average. An equivalent interpretation can be given in terms of rotational motion. A shear wave induces a rigid-body rotation of the loop without changing its perimeter. Since DAS measures changes in fiber length rather than rigid rotations, this component of the wavefield produces no strain in the fiber.

3.2 From a source to the fiber array

3.2.1 Estimation of the local fiber response

To characterize the local DAS response, we compare the amplitudes predicted by our forward model for a given source with the amplitudes recorded along the DAS array. The ratio between the two provides a proxy for local amplitude anomalies.

An example of the recorded wavefield, the corresponding forward-model prediction, and their divergence is shown in Figure 7, smoothed using the values of 3 consecutive channels. To quantify the scaling relationship between modeled and recorded amplitudes, we perform a weighted linear regression in $log - log$ space (Figure 8), where the weights are defined by the uncertainties estimated from the forward model. Prior to the regression, the measurements and their errors are median-binned along the measured-amplitude axis to homogenize the distribution of observations. The residuals are then interpreted as amplitude scaling factors, equal to the residual raised to the power of the logarithm base. To reduce uncertainty in the amplitude scaling factors, we retain the 68 out of 81 sweeps with $R^2 > 0.4$ and compute their median. The associated uncertainty is estimated using a bootstrap approach, in which random noise consistent with the standard deviation of the regression residuals is added to each realization.

Overall, the linear regression performed equally well across the different source types but not across the different source locations. Sites 8 and 9 are poorly constrained by our model while the rest are getting better as the source is further away from site 7. A summary of R^2 values by source type and site is provided in Table 1. Additionally, the SNR in many channels north of a fault that crosses the array from northwest to southeast (dashed lines in Figure 9), and also separate sites 8 and 9, was not high enough for more than 75% of the sources, hence show no residual.

Statistic	Source P	Source SL	Source ST	Site 1	Site 2	Site 3	Site 4	Site 5	Site 6	Site 7	Site 8	Site 9
Median	0.673	0.676	0.643	0.761	0.801	0.698	0.617	0.713	0.731	0.491	0.439	0.312
Std	0.207	0.244	0.147	0.050	0.069	0.128	0.109	0.200	0.121	0.239	0.175	0.140
Min	0.168	0.011	0.212	0.676	0.677	0.489	0.421	0.212	0.438	0.011	0.261	0.168
Max	0.891	0.849	0.833	0.833	0.891	0.891	0.746	0.780	0.822	0.643	0.756	0.598

Table 1 Sources and sites model statistics. Sources can be compressional (P), shear transverse (ST) and shear longitudinal (SL). The sites are visible in Figure 3.

The residuals, on the other hand, show clear anomalous regions, reaching values from 0.5 up to 0.88 in similar regions and magnitude as in Muir and Zhan (2022). When compared to the response of the P arrival of the M 4.3

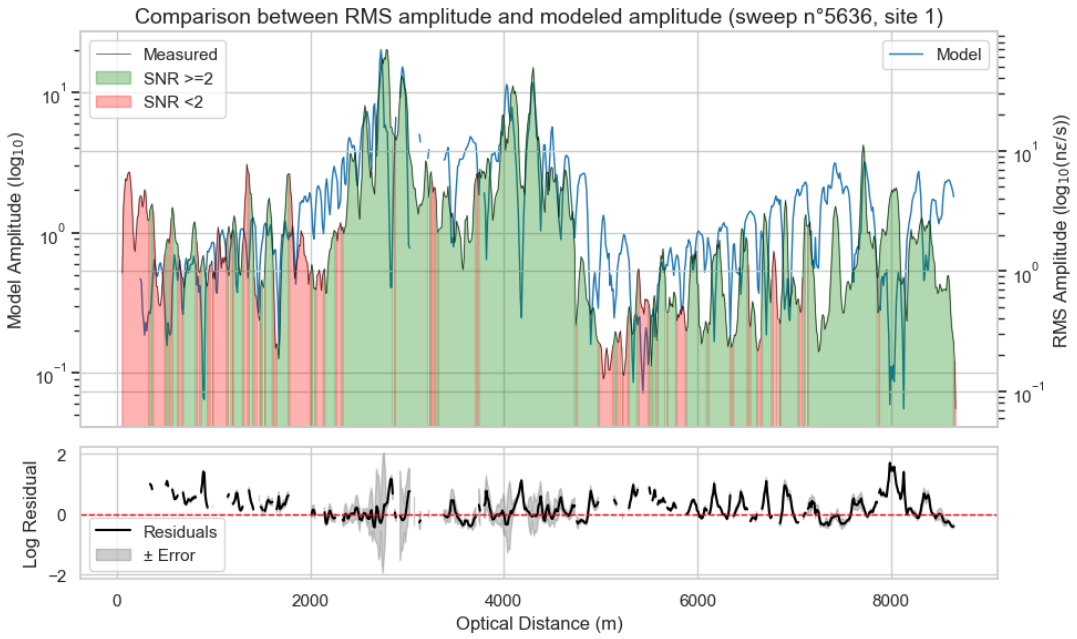

Figure 7 Comparison between modeled and measured amplitude distributions across the DAS array for sweep 5636 (site 1), and the amplitude correction associated with local site amplification. In the top panel, the modeled (forward) amplitudes are shown in blue and the measured amplitudes in black. Measurements are separated into regions with SNR > 2 in green and < 2 in red. The bottom panel shows the residuals from a linear regression, as in Figure 8. Only data with SNR > 2 are used to compute these residuals. These logarithmic residuals correspond to scaling factors associated with site-effect amplification. The gray shaded area around the log residual represents the uncertainty arising from ray-tracing errors of that scaling factor.

earthquake, similar regions are illuminated by anomalously high response. Following Wang et al. (2018), these are associated to site effects. However, an application to rescale the earthquake amplitude and recover orientation was not doable as the error level is, for most of the fiber, higher than the rescaling coefficient.

4 Discussion

4.1 The impact of fiber orientation on its sensing capacities

By creating a framework to investigate a wavefield as "seen" by DAS, we could understand the amplitude variation observed across the array. Where the prediction failed, the method highlighted local amplification in the DAS record. The spatial distribution of these amplifications coincides with the amplitude anomalies observed for an M 4.3 earthquake. Yet, we still observe discrepancies between the forward-modeled and measured amplitude patterns that do not coincide with these anomalous regions. These differences may arise from the limitations of the ray tracing, which does not account for later arrivals. At BHS these later arrivals could include reflections in between fault planes, which might be better sensed in the fiber than the direct wavefield.

We also note a significant loss of amplitude after crossing some faults, not included in the model. On the source side, the signal from the vibroseis was not always detectable across the full array, reducing the amount of usable regression points and lowering the R^2 for some of the linear regressions. Stronger sources, such as regional earthquakes, could improve the model if available in the dataset. Alternatively, ambient noise could be used, although this would be based on surface waves. Overall, the complexity of the wavefield in the geology of BHS leads to large variations between the predicted and observed signals, contributing to the generally large uncertainties on the scaling factor. The evolution of the R^2 values illustrates this behavior, increasing from 0.49 to 0.80 as the distance from the site 7, the most affected region by local amplification, increases. Developing a full-waveform model could help quantify the importance of all the elements not considered in our model in the case of a boundary-rich environment such as BHS and disentangle the respective effects of these amplifications. Also, when a correction factor is produced, we note that the residuals are tied to the average sensitivity of the array at a given frequency. This makes them unsuitable for inter-array comparisons or as an absolute amplitude correction factor.

Finally, assumptions in both our model and the criteria used to select the measured amplitudes may introduce biases in the scaling factor. On the modeling side, our angular sensitivity equations describe a plane wave measured by a linear gauge length, which we approximate as a point sensor. This approximation relies on two main assumptions. First, the plane-wave assumption implies that both the wave vector, $\vec{K}$, and the wave amplitude re-

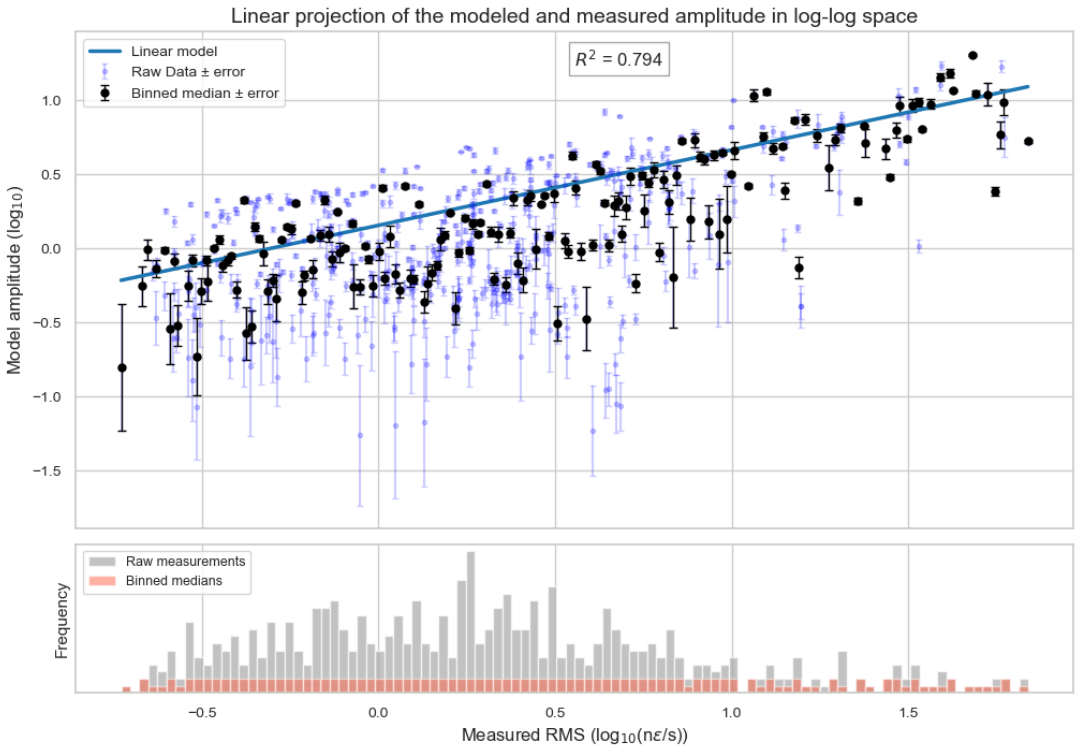

Figure 8 Extraction of amplitude scaling factors from modeled and measured amplitudes using linear regression for sweep 5636. The top panel shows a weighted linear regression in logarithmic space between measured and modeled amplitudes. The residuals relative to this regression define the amplitude scaling factors. The regression weights are given by the uncertainties from the forward model. To homogenize the measured amplitude distribution, the original data (blue) are median-binned, yielding the black points used in the regression. The bottom panel shows the density of amplitude measurements, with the original distribution in gray and the binned distribution in red.

main constant over the gauge length. In our study, the typical wavelength is approximately 120 m, which, following Zhang and Schmitt (2026), is sufficiently large relative to our 10 m gauge length to approximate the DAS channel as a point sensor. In addition, the sources are distributed across the study area, so that most measurements are obtained from relatively distant sources. Second, we assume that the gauge length is linear. This assumption breaks down at corners, where a single gauge length can encompass multiple fiber orientations and therefore exhibit a different transfer function (Kennett and Saygin, 2025). To account for those, we smooth both the modeled and measured amplitudes. In our model, this mixes the angular sensitivity between the different fiber orientations, consistent with Kennett and Saygin (2025). On the other hand, stacking the channels and the smoothing the measured amplitude reduces the importance of the corner effects. The absence of distinct anomalies at fiber corners in Figure 9 suggests that this approach is sufficient for the present analysis.

On the measurement side, we restrict the analysis to channels with an SNR greater than 2. This selection ensures that the retained amplitudes contain a measurable wavefield signal. However, it also implies that channels experiencing strong sensitivity losses, such as loops in visit chambers, are excluded from the analysis. Consequently, our analysis is efficient to quantify sensitivity gain, but not losses.

4.2 Future perspectives

For this experiment, we used a DAS sensitivity model to detect amplitude outliers and generate an amplitude correction factor. However, the travel-time grid and amplitude patterns we produce could support additional applications. For instance, when training deep neural networks for earthquake detection and phase picking, synthetic datasets could be built by convolving event waveforms with relative time and amplitude information from the model. This would allow for unbiased training regardless of the availability of earthquakes, while remaining at fairly low computational cost. At BHS, we tested the sensitivity of an existing array, but we could also evaluate hypothetical arrays and integrate these results for future deployment planning (Fichtner and Hofstede, 2023; Strutz et al., 2026). Furthermore, for any array, the DAS shadow zones could be mapped to guide the placement of seismometers to build hybrid arrays (Muir and Zhan, 2022). A deeper understanding of DAS transfer function also highlights that blind spots themselves can carry valuable information. These could be incorporated in an amplitude look-up table for

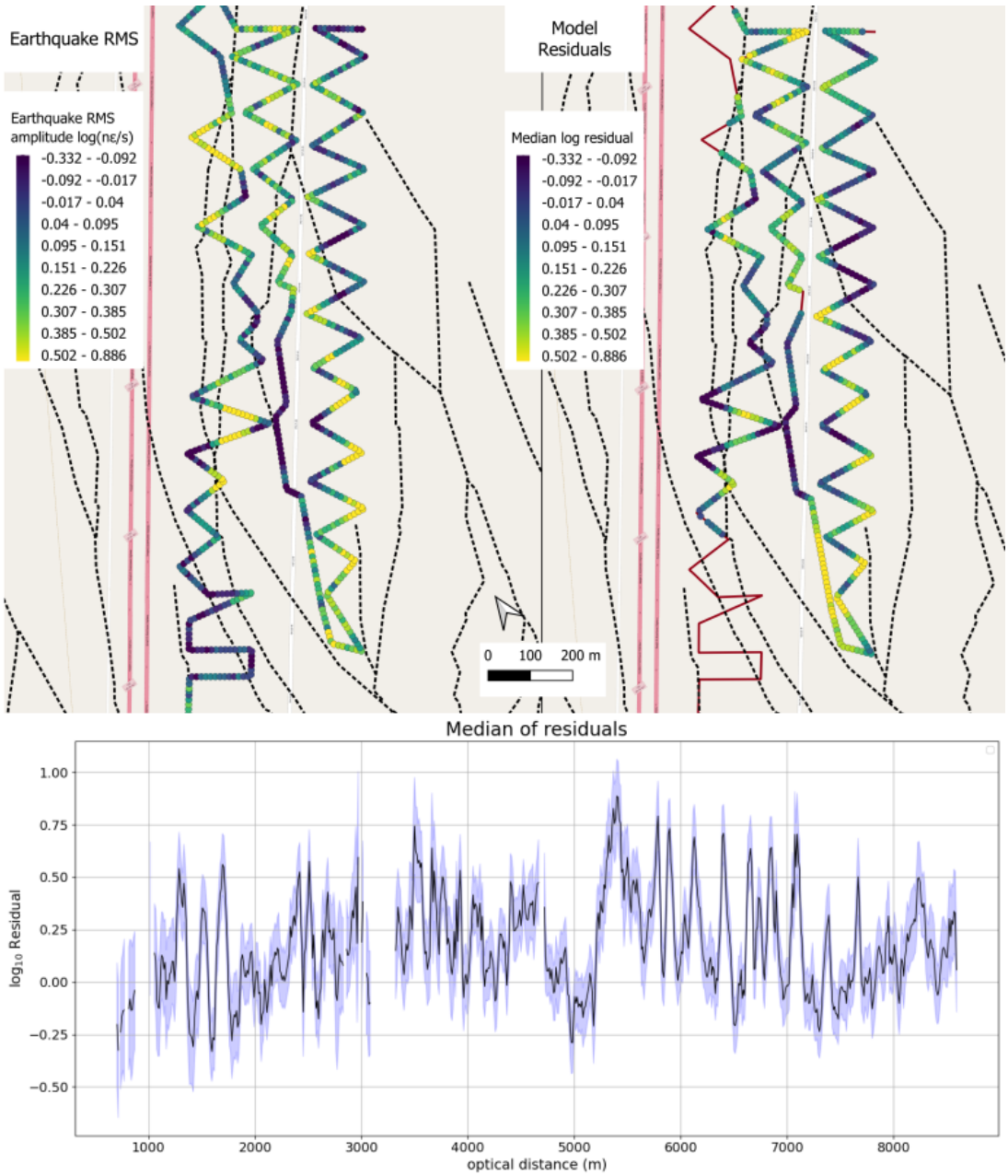

Figure 9 Comparison between the estimated site amplification factors and the measured P-wave amplitudes for the M 4.3 earthquake. In the top panel, the left plot shows the earthquake amplitude expressed as $log(n\epsilon/s)$, while the right plot shows the median of the log-residuals computed across the 9 sites. Areas with no displayed data correspond to locations where fewer than 30 sweeps had SNR > 2. The bottom panel shows the same log-residuals as a function of optical distance, along with their relative uncertainties.

pre-grid search optimization, reducing computational effort. One last application of our model is in f-k analysis to solve a problem encountered in Lindsey et al. (2017) or Hudson et al. (2021). By assigning the model's amplitude sign to the corresponding elements of the steering vector, the polarity reversal of shear waves would be accounted for, making the stacking operation constructive again. Finally, our work on the polarization filter of looped gauge lengths remains theoretical. Field deployments will be needed to validate the concept. If these proved to be efficient, these features could be integrated in new arrays for shear wave polarization analysis. Another application could be in filtering surface waves using horizontal loops. Seeing the angular sensitivity to P and SV waves but the absence of SH waves, the gauge length effect could be used as an analog filter for Love waves and omnidirectional sensors for Rayleigh waves. If proven efficient, these looped gauge length could build a bridge between rotational seismology and DAS.

5 Conclusions

In this work, we consider the impact of the fiber orientation on its capacity to record the amplitude of a body waves. Building on previous studies, we formulate a single expression for the transfer function of a linear gauge length with arbitrary dip and azimuth. Through it, we gained an understanding of the amplitude recorded by a DAS from the scale of the array to looped gauge length that could be used as shear waves polarization filters. When combining this knowledge with ray tracing tools, we could investigate the capacities across the array to recover the amplitude of a source. From the amplitude difference between the forward modeled and the recording of vibroseis, we could separate the fiber orientation and local amplification effects at low computational cost, giving us an array-specific amplitude correction factor. However, due to the complexity of the wavefield in BHS, not captured by our model, our amplitude rescaling retains large error. This forward-modeling perspective also allows us to examine the ability of a fiber segment to capture sources in its surrounding space. In particular, it emphasizes the interplay between the velocity structure and gauge length orientation. In summary, by exploiting the known directional sensitivity of DAS, we draw new insights from amplitude variations along the fiber array, treating energy loss as equally informative as energy gain in interpreting the wavefield.

Finally, from our model's time and amplitude information, we could support many new applications encompassing grid search optimizations, creation of waveform synthetics at low computational cost, and beamforming.

Acknowledgements

We thank Daniel Bowden and the Observational Seismology group at ETH Zürich for the initial discussions that inspired this project. We are also grateful to Pascale Edme for valuable insights on the free-surface effect, and to Társilo Girona for his helpful feedback on the manuscript. We also thank the reviewers for their constructive comments and suggestions, which helped improve the manuscript.

This research was supported by the Fonds de la Recherche Scientifique (FNRS, contract number FC 49429). We further acknowledge the use of `DASPy` (Hu and Li, 2024) and `PyKonal` (White et al., 2020). We also thank the developers of Python, NumPy and Matplotlib.

Data and code availability

All codes developed and used in this study—specifically those applied to the Brady Hot Springs dataset, including the implementation of a rotated Cartesian reference system—are available on Zenodo (Fontaine, 2026). A generalized version of this code with a tutorial to use it can be found in: https://github.com/olfontai/DAS_sensitivity.git. The DAS data, provided in SEGY format, were accessed through the open-source GDR repository (Feigl et al., 2016)

Competing interests

The authors declare no competition of interest.

References

Ajo-Franklin, J. B., Dou, S., Lindsey, N. J., Monga, I., Tracy, C., Robertson, M., Rodriguez Tribaldos, V., Ulrich, C., Freifeld, B., Daley, T., and Li, X. Distributed Acoustic Sensing Using Dark Fiber for Near-Surface Characterization and Broadband Seismic Event Detection. *Scientific Reports*, 9(1):1328, Feb. 2019. doi: 10.1038/s41598-018-36675-8.

Aki, K. and Richards, P. G. *Quantitative Seismology*. University Science Books, Jan. 2002.

Bakku, S. K. *Fracture characterization from seismic measurements in a borehole*. PhD Thesis, Massachusetts Institute of Technology, 2015. https://dspace.mit.edu/handle/1721.1/97331.

Benioff, H. A linear strain seismograph*. *Bulletin of the Seismological Society of America*, 25(4):283–309, Oct. 1935. doi: 10.1785/BSSA0250040283.

Capdeville, Y. and Sladen, A. DAS sensitivity to heterogeneity scales much smaller than the minimum wavelength. *Seismica*, 3(1), Jan. 2024. doi: 10.26443/seismica.v3i1.1007.

Celli, N. L., Bean, C. J., and O'Brien, G. S. Full-waveform simulation of DAS records, response and cable-ground coupling. *Geophysical Journal International*, 236(1):659–674, Jan. 2024. doi: 10.1093/gji/ggad449.

Currenti, G., Jousset, P., Napoli, R., Krawczyk, C., and Weber, M. On the comparison of strain measurements from fibre optics with a dense seismometer array at Etna volcano (Italy). *Solid Earth*, 12(4):993–1003, Apr. 2021. doi: 10.5194/se-12-993-2021.

Daley, T. M., Robertson, M., Freifeld, B. M., White, D., Miller, D. E., Herkenhoff, F., and Cocker, J. Simultaneous acquisition of distributed acoustic sensing VSP with multi-mode and single-mode fiber optic cables and 3-component geophones at the Aquistore CO2 storage site.

In *SEG Technical Program Expanded Abstracts 2014*, SEG Technical Program Expanded Abstracts, pages 5014–5018. Society of Exploration Geophysicists, Aug. 2014. doi: 10.1190/segam2014-1357.1.

Daley, T. M., Miller, D. E., Dodds, K., Cook, P., and Freifeld, B. Field testing of modular borehole monitoring with simultaneous distributed acoustic sensing and geophone vertical seismic profiles at Citronelle, Alabama. *Geophysical Prospecting*, 64(5):1318–1334, 2016. doi: 10.1111/1365-2478.12324.

Feigl, K. L. Material Properties for Brady Hot Springs Nevada USA from PoroTomo Project. Technical Report 1124, USDOE Geothermal Data Repository (United States); Univ. of Wisconsin, Madison, WI (United States), Mar. 2019. doi: 10.15121/1501544.

Feigl, K. L., Reinisch, E., Patterson, J., Jreij, S., Parker, L., Nayak, A., Zeng, X., Cardiff, M., Lord, N. E., Fratta, D., Thurber, C., Wang, H., Robertson, M., Coleman, T., Miller, D. E., Spielman, P., Akerley, J., Kreemer, C., Morency, C., Matzel, E., Trainor-Guitton, W., and Davatzes, N. Geothermal Data Repository, 2016. doi: 10.15121/1778858.

Fichtner, A. and Hofstede, C. A simple algorithm for optimal design in distributed fibre-optic sensing. *Geophysical Journal International*, 233(1):229–233, Apr. 2023. doi: 10.1093/gji/ggac458.

Fichtner, A., Hofstede, C., Kennett, B. L. N., Nymand, N. F., Lauritzen, M. L., Zigone, D., and Eisen, O. Fiber-Optic Airplane Seismology on the Northeast Greenland Ice Stream. *The Seismic Record*, 3(2):125–133, May 2023. doi: 10.1785/0320230004.

Fichtner, A., Walter, F., Brisbourne, A., Booth, A. D., Kendall, J. M., Hudson, T. S., Paitz, P., and Lipovsky, B. P. Fibre-optic exploration of the cryosphere. *Geophysical Journal International*, 244(2):ggaf489, Feb. 2026. doi: 10.1093/gji/ggaf489.

Fontaine, O. Understanding fiber-optic sensitivity to a wavefield: A framework to separate site amplification from orientation effects [software], 2026. doi: 10.5281/zenodo.18863370.

Han, L., Wong, J., and Bancroft, J. C. Time picking and random noise reduction on microseismic data. CREWES Research Reports, 2009. https://api.semanticscholar.org/CorpusID:221208031.

Hartog, A., Frignet, B., Mackie, D., and Clark, M. Vertical seismic optical profiling on wireline logging cable. *Geophysical Prospecting*, 62(4): 693–701, May 2014. doi: 10.1111/1365-2478.12141.

Hu, M. and Li, Z. DASPy: A Python Toolbox for DAS Seismology. *Seismological Research Letters*, 95(5):3055–3066, July 2024. doi: 10.1785/0220240124.

Hudson, T. S., Brisbourne, A., Walter, F., Gräff, D., White, R., and Smith, A. Icequake Source Mechanisms for Studying Glacial Sliding. *Journal of Geophysical Research: Earth Surface*, 125, Nov. 2020. doi: 10.1029/2020JF005627.

Hudson, T. S., Baird, A. F., Kendall, J. M., Kufner, S. K., Brisbourne, A. M., Smith, A. M., Butcher, A., Chalari, A., and Clarke, A. Distributed Acoustic Sensing (DAS) for Natural Microseismicity Studies: A Case Study From Antarctica. *Journal of Geophysical Research: Solid Earth*, 126(7):e2020JB021493, 2021. doi: 10.1029/2020JB021493.

Hudson, T. S., Klaasen, S., Fontaine, O., Bacon, C. A., Jónsdóttir, K., and Fichtner, A. Towards a widely applicable earthquake detection algorithm for fibreoptic and hybrid fibreoptic-seismometer networks. *Geophysical Journal International*, 240(3):1965–1985, Mar. 2025a. doi: 10.1093/gji/ggae459.

Hudson, T. S., Stork, A., Muir, J., and Fichtner, A. Unlocking DAS amplitude information through coherency coupling quantification. *Seismica*, 4(1), Mar. 2025b. doi: 10.26443/seismica.v4i1.1488.

Ichinose, G. A., Mellors, R. J., Barno, J. G., and Gok, R. Comparisons Between Array Derived Dynamic Strain Rate (ADDS) and Fiber-Optic Distributed Acoustic Sensing (DAS) Strain Rate. *Journal of Geophysical Research: Solid Earth*, 127(12):e2022JB025101, 2022. doi: 10.1029/2022JB025101.

Jiang, K., Liang, L., Tong, X., Zeng, F., and Hu, X. How the Material Characteristics of Optical Fibers and Soil Influence the Measurement Results of Distributed Acoustic Sensing. *Sensors*, 23(17):7340, Jan. 2023. doi: 10.3390/s23177340.

Jousset, P., Reinsch, T., Ryberg, T., Blanck, H., Clarke, A., Aghayev, R., Hersir, G. P., Henninges, J., Weber, M., and Krawczyk, C. M. Dynamic strain determination using fibre-optic cables allows imaging of seismological and structural features. *Nature Communications*, 9(1):2509, July 2018. doi: 10.1038/s41467-018-04860-y.

Jousset, P., Currenti, G., Murphy, S., Eibl, E. P. S., Caudron, C., Retailleau, L., Wollin, C., Klaasen, S., Nishimura, T., Fichtner, A., Spica, Z., Lemarchand, A., and Krawczyk, C. Fiber Optic Sensing for Volcano Monitoring and Imaging Volcanic Processes. In Spica, Z. and Caudron, C., editors, *Modern Volcano Monitoring*, pages 509–567. Springer Nature Switzerland, Cham, 2025. doi: 10.1007/978-3-031-86841-2_17.

Kennett, B. L. N. The seismic wavefield as seen by distributed acoustic sensing arrays: local, regional and teleseismic sources. *Proceedings of The Royal Society of London*, 478:0812, Feb. 2022. doi: 10.1098/rspa.2021.0812.

Kennett, B. L. N. A Guide to the Seismic Wavefield as seen by DAS. Aug. 2024. doi: 10.25911/ACGD-6161.

Kennett, B. L. N. and Saygin, E. The Effect of Sharp Bends and Cable Coupling on DAS Recording in an Urban Environment. *The Seismic Record*, 5(1):118–126, Jan. 2025. doi: 10.1785/0320240045.

Kuvshinov, B. Interaction of helically wound fibre-optic cables with plane seismic waves. *Geophysical Prospecting*, 64(3):671–688, 2016. doi: 10.1111/1365-2478.12303.

Lindsey, N. J., Martin, E. R., Dreger, D. S., Freifeld, B., Cole, S., James, S. R., Biondi, B. L., and Ajo-Franklin, J. B. Fiber-optic network observations of earthquake wavefields. *Geophysical Research Letters*, 44(23):11,792–11,799, 2017. doi: 10.1002/2017GL075722.

Lindsey, N. J., Rademacher, H., and Ajo-Franklin, J. B. On the Broadband Instrument Response of Fiber-Optic DAS Arrays. *Journal of*

Geophysical Research: Solid Earth, 125(2):e2019JB018145, 2020. doi: 10.1029/2019JB018145.

Lior, I., Sladen, A., Rivet, D., Ampuero, J.-P., Hello, Y., Becerril, C., Martins, H. F., Lamare, P., Jestin, C., Tsagkli, S., and Markou, C. On the Detection Capabilities of Underwater Distributed Acoustic Sensing. *Journal of Geophysical Research: Solid Earth*, 126(3):e2020JB020925, 2021. doi: 10.1029/2020JB020925.

Liu, Y. and Schmitt, D. R. The Transition Between the Scale Domains of Ray and Effective Medium Theory and Anisotropy: Numerical Models. *pure and applied geophysics*, 163(7):1327–1349, July 2006. doi: 10.1007/s00024-006-0075-5.

Lokmer, I. and Bean, C. J. Properties of the near-field term and its effect on polarisation analysis and source locations of long-period (LP) and very-long-period (VLP) seismic events at volcanoes. *Journal of Volcanology and Geothermal Research*, 192(1):35–47, Apr. 2010. doi: 10.1016/j.jvolgeores.2010.02.008.

Luo, B., Jin, G., and Stanek, F. Near-field strain in distributed acoustic sensing-based microseismic observation. *Geophysics*, 86(5):P49–P60, Aug. 2021. doi: 10.1190/geo2021-0031.1.

Ma, K.-F., von Specht, S., Kuo, L.-W., Huang, H.-H., Lin, C.-R., Lin, C.-J., Ku, C.-S., Wu, E.-S., Wang, C.-Y., Chang, W.-Y., and Jousset, P. Broadband strain amplification in an asymmetric fault zone observed from borehole optical fiber and core. *Communications Earth & Environment*, 5(1):1–13, July 2024. doi: 10.1038/s43247-024-01558-6.

Martin, E., Lindsey, N., Ajo-Franklin, J., and Biondi, B. Introduction to Interferometry of Fiber-Optic Strain Measurements. pages 111–129. Dec. 2021. doi: 10.1002/9781119521808.ch9.

Mateeva, A., Lopez, J., Potters, H., Mestayer, J., Cox, B., Kiyashchenko, D., Wills, P., Grandi, S., Hornman, K., Kuvshinov, B., Berlang, W., Yang, Z., and Detomo, R. Distributed acoustic sensing for reservoir monitoring with vertical seismic profiling. *Geophysical Prospecting*, 62(4): 679–692, 2014. doi: 10.1111/1365-2478.12116.

Matzel, E., Zeng, X., Thurber, C., Y.Luo, and Morency, C. Seismic interferometry using the dense array at the brady geothermal field. Feb. 2017.

Muir, J. B. and Zhan, Z. Wavefield-based evaluation of DAS instrument response and array design. *Geophysical Journal International*, 229 (1):21–34, Apr. 2022. doi: 10.1093/gji/ggab439.

Nakano, M., Ichihara, M., Suetsugu, D., Ohminato, T., Ono, S., Vaiomounga, R., Kula, T., and Shinohara, M. Monitoring volcanic activity with distributed acoustic sensing using the Tongan seafloor telecommunications cable. *Earth, Planets and Space*, 76(1):25, Feb. 2024. doi: 10.1186/s40623-024-01972-2.

Nishimura, T., Emoto, K., Nakahara, H., Miura, S., Yamamoto, M., Sugimura, S., Ishikawa, A., and Kimura, T. Source location of volcanic earthquakes and subsurface characterization using fiber-optic cable and distributed acoustic sensing system. *Scientific Reports*, 11(1): 6319, Mar. 2021. doi: 10.1038/s41598-021-85621-8.

Noe, S., Tuinstra, K. B., Klaasen, S., Krischer, L., and Fichtner, A. Theoretical background for full-waveform inversion with distributed acoustic sensing and integrated strain sensing. *Geophysical Journal International*, 244(1):ggaf406, Jan. 2026. doi: 10.1093/gji/ggaf406.

Paitz, P., Edme, P., Gräff, D., Walter, F., Doetsch, J., Chalari, A., Schmelzbach, C., and Fichtner, A. Empirical Investigations of the Instrument Response for Distributed Acoustic Sensing (DAS) across 17 Octaves. *Bulletin of the Seismological Society of America*, 111(1):1–10, Oct. 2020. doi: 10.1785/0120200185.

Rawlinson, N., Hauser, J., and Sambridge, M. Seismic ray tracing and wavefront tracking in laterally heterogeneous media. In Dmowska, R., editor, *Advances in Geophysics*, volume 49, pages 203–273. Elsevier, Jan. 2008. doi: 10.1016/S0065-2687(07)49003-3.

Siler, D. L. and Pepin, J. D. 3-D Geologic Controls of Hydrothermal Fluid Flow at Brady geothermal field, Nevada, USA. *Geothermics*, 94: 102112, July 2021. doi: 10.1016/j.geothermics.2021.102112.

Strutz, D., Kiers, T., and Curtis, A. Single and multi-objective optimization of distributed acoustic sensing cable layouts for geophysical applications. *Geophysical Journal International*, 245(1):ggag058, Apr. 2026. doi: 10.1093/gji/ggag058.

Vantassel, J. P., Cox, B. R., Hubbard, P. G., Yust, M., Menq, F., Spikes, K., and Fratta, D. Effectiveness of Distributed Acoustic Sensing for Acquiring Surface Wave Dispersion Data Using Multichannel Analysis of Surface Waves. In Wang, L., Zhang, J.-M., and Wang, R., editors, *Proceedings of the 4th International Conference on Performance Based Design in Earthquake Geotechnical Engineering (Beijing 2022)*, pages 1000–1008. Springer International Publishing, Cham, 2022. doi: 10.1007/978-3-031-11898-2_77.

Vera Rodriguez, I. and Wuestefeld, A. Strain microseismics: Radiation patterns, synthetics, and moment tensor resolvability with distributed acoustic sensing in isotropic media. *Geophysics*, 85(3):KS101–KS114, Apr. 2020. doi: 10.1190/geo2019-0373.1.

Walter, F., Gräff, D., Lindner, F., Paitz, P., Köpfli, M., Chmiel, M., and Fichtner, A. Distributed acoustic sensing of microseismic sources and wave propagation in glaciated terrain. *Nature Communications*, 11(1):2436, May 2020. doi: 10.1038/s41467-020-15824-6.

Wang, H. F., Zeng, X., Miller, D. E., Fratta, D., Feigl, K. L., Thurber, C. H., and Mellors, R. J. Ground motion response to an ML 4.3 earthquake using co-located distributed acoustic sensing and seismometer arrays. *Geophysical Journal International*, 213(3):2020–2036, June 2018. doi: 10.1093/gji/ggy102.

White, M. C. A., Fang, H., Nakata, N., and Ben-Zion, Y. PyKonal: A Python Package for Solving the Eikonal Equation in Spherical and Cartesian Coordinates Using the Fast Marching Method. *Seismological Research Letters*, 91(4):2378–2389, June 2020. doi: 10.1785/0220190318.

Xie, T., Zhang, C.-C., Shi, B., Li, J.-P., and Zhang, T.-Y. Could fiber strains affect DAS amplitude response? *Measurement*, 189:110428, Feb. 2022. doi: 10.1016/j.measurement.2021.110428.

Yin, J., Soto, M. A., Ramírez, J., Kamalov, V., Zhu, W., Husker, A., and Zhan, Z. Real-Data Testing of Distributed Acoustic Sensing for Offshore

Earthquake Early Warning. *The Seismic Record*, 3(4):269–277, Oct. 2023. doi: 10.1785/0320230018.

Zhang, O. and Schmitt, D. R. Distributed Acoustic Sensing (DAS) Waveforms: Effects of Source Signature, Geometry, and Attenuation. *Earth and Space Science*, 13(7):e2025EA004948, 2026. doi: 10.1029/2025EA004948.

The article *Understanding fiber-optic sensitivity to a wavefield: A framework to separate site amplification from orientation effects* © 2026 by Olivier Fontaine is licensed under CC BY 4.0.